AFRL-RX-WP-TP-2009-4209

STRESS GRADIENT INDUCED STRAIN LOCALIZATION IN METALS: HIGH RESOLUTION STRAIN CROSS SECTIONING VIA SYNCHROTRON X-RAY DIFFRACTION (POSTPRINT)

M. Croft, N. Jisrawi, Z. Zhong, K. Horvath, R.L. Holtz, M. Shepard, M. Lakshmipathy, K. Sadananda, J. Skaritka, V. Shukla, R. K. Sadangi, and T. Tsakalakos

Metals Branch
Metals, Ceramics, and NDE Division

APRIL 2008

AIR FORCE RESEARCH LABORATORY
MATERIALS AND MANUFACTURING DIRECTORATE
WRIGHT-PATTERSON AIR FORCE BASE, OH 45433-7750
AIR FORCE MATERIEL COMMAND
UNITED STATES AIR FORCE

REPORT DOCUMENTATION PAGE

Form Approved
OMB No. 0704-0188

The public reporting burden for this collection of information is estimated to average 1 hour per response, including the time for reviewing instructions, searching existing data sources, searching existing data sources, gathering and maintaining the data needed, and completing and reviewing the collection of information. Send comments regarding this burden estimate or any other aspect of this collection of information, including suggestions for reducing this burden, to Department of Defense, Washington Headquarters Services, Directorate for Information Operations and Reports (0704-0188), 1215 Jefferson Davis Highway, Suite 1204, Arlington, VA 22202-4302. Respondents should be aware that notwithstanding any other provision of law, no person shall be subject to any penalty for failing to comply with a collection of information if it does not display a currently valid OMB control number. **PLEASE DO NOT RETURN YOUR FORM TO THE ABOVE ADDRESS**.

1. REPORT DATE *(DD-MM-YY)*	2. REPORT TYPE	3. DATES COVERED *(From - To)*
April 2008	Journal Article Postprint	

4. TITLE AND SUBTITLE
STRESS GRADIENT INDUCED STRAIN LOCALIZATION IN METALS: HIGH RESOLUTION STRAIN CROSS SECTIONING VIA SYNCHROTRON X-RAY DIFFRACTION (POSTPRINT)

5a. CONTRACT NUMBER
In-house

5b. GRANT NUMBER

5c. PROGRAM ELEMENT NUMBER
62102F

6. AUTHOR(S)
M. Croft, N. Jisrawi, K. Horvath, V. Shukla, R.K. Sadangi, and T. Tsakalakos (Rutgers University)
Z. Zhong and J. Skaritka (Brookhaven National Laboratory)
R.L. Holtz (Naval Research Laboratory)
M. Shepard (AFRL/RXLMN)
M. Lakshmipathy (Zygo Corporation)
K. Sadananda (Technical Data Analysis, Inc.)

5d. PROJECT NUMBER
4347

5e. TASK NUMBER
RG

5f. WORK UNIT NUMBER
M02R3000

7. PERFORMING ORGANIZATION NAME(S) AND ADDRESS(ES)
Rutgers University

Brookhaven National Laboratory

Naval Research Laboratory

Metals Branch (AFRL/RXLMN)
Metals, Ceramics, and NDE Division
Materials and Manufacturing Directorate
Wright-Patterson Air Force Base, OH 45433-7750
Air Force Materiel Command, United States Air Force

Zygo Corporation

Technical Data Analysis, Inc.

8. PERFORMING ORGANIZATION REPORT NUMBER
AFRL-RX-WP-TP-2009-4209

9. SPONSORING/MONITORING AGENCY NAME(S) AND ADDRESS(ES)
Air Force Research Laboratory
Materials and Manufacturing Directorate
Wright-Patterson Air Force Base, OH 45433-7750
Air Force Materiel Command
United States Air Force

10. SPONSORING/MONITORING AGENCY ACRONYM(S)
AFRL/RXLMN

11. SPONSORING/MONITORING AGENCY REPORT NUMBER(S)
AFRL-RX-WP-TP-2009-4209

12. DISTRIBUTION/AVAILABILITY STATEMENT
Approved for public release; distribution unlimited.

13. SUPPLEMENTARY NOTES
Journal article published in *Journal of Engineering Materials and Technology*, Vol. 130, April 2008. PAO Case Number: WPAFB 07-0684; Clearance Date: 12 Dec 2007. © 2008 ASME. The U.S. Government is joint author of this work and has the right to use, modify, reproduce, release, perform, display, or disclose the work. Paper contains color.

14. ABSTRACT
Strain localization in the presence of a stress gradient is a phenomenon common to many systems described by continuum mechanics. Variations of this complex phenomenon lead to interesting nonlinear effects in materials/engineering science as well as in other fields. Here, the synchrotron based energy dispersive x-ray diffraction (EDXRD) technique is used for high spatial resolution profiling of both compression and tension induced strain localization in important materials/engineering problems. Specifically, compression induced strain localization in shot peened materials and tension induced strain localization in the plastic zones adjoining the faces of a fatigue crack are profiled. The utility of the EDXRD synchrotron technique for nondestructively cross-sectioning strain variations on small length scales is described. While the strain field profiling relies on the shift of the Bragg lines, the data show that plastic deformation regions can also consistently be seen in the broadening of the Bragg peaks through the full width at half maximum parameter.

15. SUBJECT TERMS
x-ray diffraction, nondestructive evaluation, residual stress, metallic materials, plastic collapse

16. SECURITY CLASSIFICATION OF:			17. LIMITATION OF ABSTRACT:	18. NUMBER OF PAGES	19a. NAME OF RESPONSIBLE PERSON (Monitor)
a. REPORT	**b. ABSTRACT**	**c. THIS PAGE**	SAR	16	James L. Larsen
Unclassified	Unclassified	Unclassified			**19b. TELEPHONE NUMBER** *(Include Area Code)* N/A

Standard Form 298 (Rev. 8-98)
Prescribed by ANSI Std. Z39-18

M. Croft
Department of Physics Astronomy,
Rutgers University,
Piscataway, NJ 08854;
National Synchrotron Light Source,
Brookhaven National Laboratory,
Upton, NY 11973

N. Jisrawi
Materials Science and Engineering Department,
Rutgers University,
Piscataway, NJ 08854;
Department of Basic Sciences,
University of Sharjah,
P.O. Box. 27272,
Sharjah, United Arab Emirates

Z. Zhong
National Synchrotron Light Source,
Brookhaven National Laboratory,
Upton, NY 11973

K. Horvath
Department of Physics Astronomy,
Rutgers University,
Piscataway, NJ 08854

R. L. Holtz
Materials Science & Technology Division,
Naval Research Laboratory,
4555 Overlook Avenue, SW,
Washington, DC 20375

M. Shepard
Materials and Manufacturing Directorate,
Air Force Research Laboratory,
WPAFB, OH 45433-7817

M. Lakshmipathy
Zygo Corporation,
Laurel Brook Road,
Middlefield, CT 06455

K. Sadananda
Technical Data Analysis, Inc.,
Falls Church, VA 22046

J. Skaritka
National Synchrotron Light Source,
Brookhaven National Laboratory,
Upton, NY 11973

V. Shukla

R. K. Sadangi

T. Tsakalakos
Materials Science and Engineering Department,
Rutgers University,
Piscataway, NJ 08854

Stress Gradient Induced Strain Localization in Metals: High Resolution Strain Cross Sectioning via Synchrotron X-Ray Diffraction

Strain localization in the presence of a stress gradient is a phenomenon common to many systems described by continuum mechanics. Variations of this complex phenomenon lead to interesting nonlinear effects in materials/engineering science as well as in other fields. Here, the synchrotron based energy dispersive x-ray diffraction (EDXRD) technique is used for high spatial resolution profiling of both compression and tension induced strain localization in important materials/engineering problems. Specifically, compression induced strain localization in shot peened materials and tension induced strain localization in the plastic zones adjoining the faces of a fatigue crack are profiled. The utility of the EDXRD synchrotron technique for nondestructively cross-sectioning strain variations on small length scales (down to $10-20~\mu m$) is described. While the strain field profiling relies on the shift of the Bragg lines, the data show that plastic deformation regions can also consistently be seen in the broadening of the Bragg peaks through the full width at half maximum parameter. Quantitative correlations between the synchrotron based x-ray determined deformations and surface deformations, as measured by optical surface height profiling, are also made. [DOI: 10.1115/1.2840962]

Keywords: C. x-ray diffraction, nondestructive evaluation, B. residual stress, metallic materials, plastic collapse

1 Introduction

The phenomenon of strain localization in the strongly nonlinear deformation regime of continuum mechanics problems is important in fields as diverse as general relativity/cosmology, biology, geology, and materials science/mechanics [1–4]. It would be extraordinarily useful, but rarely realizable, in many of these diverse problems if one could experimentally perform local profiling of the underlying strain fields on the relevant length scales in order to construct and verify theoretical modeling. In recent years, high energy synchrotron radiation-based x-ray diffraction methods have been evolving, which allow such strain field profiling/mapping of local strain field gradients on the germane short length scales deep in the interior of materials [5–13]. The ability to nondestructively cross section the strain response traversing a steep strain gradient is now highly feasible for certain classes of problems in elastoplastic deformation of solids. In this paper, we employ one of these high energy synchrotron techniques, energy dispersive x-ray diffraction (EDXRD) [5–11], to precisely profile the relevant local strain field gradients in two important materials science/engineering problems. Specifically, we address the local, anisotropic strain fields in metallic specimens driven to localized plastic deformation under compression (induced by shot peening) and under tension (induced by the previous passage of a fatigue crack tip). Interestingly, these two strain localization examples are diametrically opposed, not just in the compression-tension sense but also in that the former is a processing intervention designed to combat the component life limiting effects of the latter (fatigue cracking). Together the shot peening and fatigue crack strain localization examples provided excellent vehicles with which to illustrate the utility, flexibility, and power of the EDXRD strain profiling method and its application to important duty life materials/engineering problems. In addition, complementary surface-height profiling measurements, reflecting the free boundary evidence for the interior strain localization processes, will be presented.

Before proceeding with the discussion of the EDXRD technique, we wish to note other recently developed synchrotron-based techniques aimed at the nondestructive quantification of the micromechanical state in polycrystalline materials both at the single-grain and grain-aggregate scales. Haeffner et al. [14] reviewed a number of high-energy, constant wave length techniques exploiting angle dispersive area detectors and the merits of various synchrotron sources. Margulies et al. [15] and Martins et al. [16] discussed such constant wavelength techniques developed to measure the evolution of the full three-dimensional (3D) strain tensor for embedded grains subject to in situ deformation. While the full strain tensor allows for unambiguous calculation of corresponding stresses, these techniques typically lack spatial depth resolution and are limited to measuring populations of about ten grains. Behnken et al. [17], Wang et al. [18], and Bernier and Miller [19] have outlined methodologies for calculating aggregate-averaged, orientation-dependent strain/stress tensor fields from powder diffraction data. Miller et al. [20] have presented a methodology for measuring lattice strain poll figures under in situ loading in multiphase alloys. Han and Dawson [21] and Barton and Dawson [22] also discussed strain distributions in multiphase alloys. In terms of high-resolution spatial profiling and mapping of lattice strains using constant wavelength techniques, the work of Jones et al. [12] and Martins et al. [13] should be noted. In particular, the use of a conical slit system provides through-sample depth resolution in the latter of these studies [13].

Many of the above constant wavelength techniques are substantially more powerful in elucidating the full local strain tensor on a much finer scale than the ones discussed in this paper. The use of white-beam EDXRD strain profiling/mapping has been reported by number of groups in the past [5–11]. This simpler technique is less sensitive to instrument geometry/setup, and allows substantial flexibility for profiling a wide class of materials of interest in engineering problems where high spatial resolution and x-ray penetration power are required. Although the EDXRD technique measures only one scattering vector (strain component) per sample orientation, it is well suited to doing profiling measurements where spatially correlation of lattice strain measurements to material inhomogeneities is desired (e.g., cracks or peened surfaces). Moreover, the simplicity of the method allows one to measure other strain components with relatively simple sample realignment. It should be noted that the spatial resolution reported in this paper is, to the authors' knowledge, the highest achieved for EDXRD strain profiling.

For heuristic purposes, it is useful to mention the specific example of strain localization and plastic deformation in a metal specimen subjected to an increasing uniaxial tensile stress [23]. Under small loads, the deformation response is linear elongation along the load direction, accompanied by a transverse (volume conserving) Poisson effect contraction. Larger stresses lead to a homogeneous breakdown (yielding) of the material with permanent plastic flow. At a still larger stresses, an inhomogeneous concentration of the plastic deformation (strain localization) onsets in which longitudinal elongation and transverse contraction (necking) change the specimen geometry in a specific localized region (typically near a stress concentrating defect or test specimen notch). Eventually, increased loading will lead to fracture, but with the necking region still evidenced adjacent to the fracture surfaces. Under compressive loading, a similar sequence occurs with the plastic deformation in the strain localization regime exhibiting a bulging (rather than necking) effect.

2 Experimental Methods

Energy Dispersive X-Ray Diffraction EDXRD measurements used for this work were performed at the Brookhaven National Synchrotron Light Source (NSLS) on the superconducting wiggler beamline X17-B1. The experimental setup, described in more details elsewhere [5–7], involves "white beam" incident radiation with scattering at a fixed angle 2θ. The energies E of the scattered Bragg peaks are given by $E = b/[d_{hkl}\sin(\theta)]$, where d_{hkl} is the spacing associated with a specific interatomic plane labeled by its Miller indices $\{hkl\}$. Here, $b = hc/2$, where h is Planck's constant and c is the speed of light. In the conventional units, where d_{hkl} is measured in angstroms and E in keV one has $b = 6.199$ Å keV [5–11]. In this work, the variation with position of the interatomic spacing (d) of a single Bragg line was used to determined the strain $\varepsilon = [(d - d_0)/d_0] = [(E_0 - E)/E_0]$ variation. Here, E is the fitted energy of the Bragg line, and the reference d_0 (and E_0) represent the stress-free lattice spacing (Bragg line energy). For the fatigue crack sample, d_0 (and E_0) were determined by the Bragg line energy far from the crack [5–7]. For the shot peened samples, d_0 (and E_0) were determined by the condition that the net stress across the entire line profile of the specimen be balanced (i.e., zero total force on the specimen). In the 4140- and 1070-steel measurements discussed here, the bcc Fe $\{321\}$ Bragg line was used to determine the strain variation. It should be noted that in the results for ε_{11} in the 1070-steel specimen, a weighted average of seven to ten bcc-Fe Bragg lines was used with essentially identical results [5]. (Here, the conventions of x_3 normal to and x_1 in the shot peened surface are followed, as discussed at length below.) Indeed, the use of multiple Bragg lines for strain determination has been used on a number of systems both by our group [5] and others [8–10].

While the spatial variation of the fitted centroid of the Bragg line is used to profile the strain variation, the fitted full width at half maximum (FWHM) of the Bragg line also provides useful material information. In EDXRD, the Bragg line FWHM is nu-

2

merically dominated by a large, but highly stable, electronic broadening (proportional to the energy). The stability of this electronic broadening effect allows one to probe variations in the coherent X-ray scattering domain size (coupled to but smaller than the grain size) and the state of microstrain [24–26]. Finally, it should be noted that a contribution to the Bragg line FWHM can also arise from the gradient of the strain within the diffraction volume.

The hcp α-Ti {110} Bragg line was used for the Ti-6Al-4V measurements. It should be noted that in the conversion between the strain results and the stress evaluations, the approximation of using the bulk elastic constants has been made. The elastic constants for specific crystalline plane directions, labeled by the Miller indices {hkl}, will vary [27]; however, this variation is typically modest and has been determined experimentally in only a limited number of systems. The intrinsically multiphase character of the Ti-6Al-4V alloy of course raises the potential important question of stress distribution among its components. In this work, only the hcp-Ti phase Bragg line has been used as a marker in strain profiling. A more detailed study comparing the hcp and fcc phase responses is clearly called for but is beyond the scope of the present work. Both these strain anisotropy and two-phase issues do not alter the central thrust of this paper illustrating the potential of the EDXRD techniques discussed here.

For the strain experiments (consider ε_{33} in the shot peened materials for specificity) discussed here, the orientation of the sample x_3 direction (normal to the peened surface) deviates by the angle θ (3 deg) from the scattering vector direction. Hence, strain measured in this case technically deviates from the true ε_{33} by a factor of $\sin(\theta)$, which entails less than 2% systematic error and is negligible compared to other sources of errors in the experiment. Rotation of the sample by θ would remove this systematic error; however, this would entail some sacrifice of the high spatial resolution achievable by aligning the incident beam parallel to the peened or crack face surfaces in the specimens studied.

The incident and diffracted beams were each collimated by two 10 mm thick Ta slits, thereby defining the size of the gauge volume (see Fig. 3(b) below). For the shot peened materials studied, the strain profile directions were from surface to surface through the interior of the specimen. For the fatigue crack study, the profile perpendicularly crossed the crack in the center (2 mm from each surface) of the 4 mm thick specimen [6,7].

Optical surface height profiling measurements on the plastically deformed regions in these materials have been performed using a Zygo Inc. New View 5200 optical profiler. Discussion of white light optical surface profiling can be found in Ref. [28]. Since the central focus of our studies is the synchrotron based x-ray profiling results, the surface profile measurements are presented in an appendix. The surface profile measurements are important because they provide a quantitative visualization of the deformations that are accessible to in-house measurements on structural specimens. Indeed, as will be seen below, the spatial scales of the surface deformations correlate well with the detailed interior strain field profiles.

Materials. The Ti-6Al-4V alloy specimen (where the 6Al and 4V are wt % constituents) was a $23 \times 23 \times 5$ mm^3 placket peened on both large surface area sides for symmetry. The SAE 1070 carbon spring steel had (by definition) ~0.7 wt % C and ~0.7 wt % Mn and was $25 \times 75 \times 4$ mm^3. The SAE 4140 Mo-steel specimen had the specified nominal compositions of ~0.4 wt % C, ~0.7 wt % Mn, ~0.9 wt % Cr, and ~0.2 wt % Mo and was $25 \times 75 \times 3$ mm^3. The normalized 4140-steel specimen discussed here was cut into a single edge notched geometry, as discussed previously [6,7]. It was then fatigued with a constant amplitude loading with the maximum-minimum excursion in the tip stress intensity factor being $K_{max} = 49.8$ MPa m$^{1/2}$ to $K_{max} = 5$ MPa m$^{1/2}$.
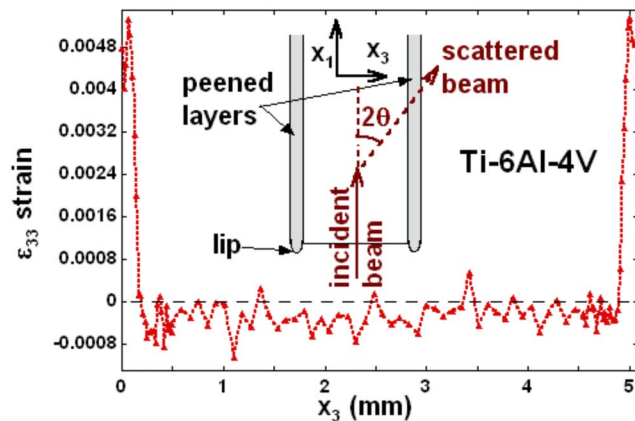
Fig. 1 Strain profile of ε_{33} across the entire thickness of a Ti-6A1-4V double-sided shot peened specimen. The inset shows schematic of the X-ray scattering geometry along with the definition of the coordinate directions. Note the schematic representation of the lip, which was optically profiled and is shown in Figs. 7(c) and 8.

3 Results and Discussion

3.1 Compressive Stress Material Breakdown: Shot Peening. Since antiquity, it has been empirically recognized that surface hardness/durability could be enhanced by a number of impact-cold-working techniques [29] (e.g., hammering). Of these processes, shot peening has found the most pervasive modern usage. Shot peening the surfaces of structural materials (such as engine components) dates back to the early 1900s [29–32] and involves surface bombardment with small, hard shot. In the Appendix, the surface cratering produced by this bombardment is pictured in Fig. 6(a) and the quantitative profiling of the surface deformation is shown in Figs. 7(a) and 7(b). The high velocity impact of the shot causes a local transient compression well beyond the material's yield strength [30–32]. By the work energy theorem, the kinetic energy of the shot is partially converted into localized plastic flow laterally away from the impact crater center [31,32]. Indeed, this lateral plastic flow creates a discernible protruding lip on the edge of a shot peened specimen. In the Appendix, a picture of this lip is shown in Fig. 6(c) and quantitative surface profiles of such lips are shown in Figs. 7(c) and 8. This lateral plastic flow creates a region of high dislocation density on top of the underlying bulk material and yields a layer with compressive residual stresses. This compressive layer greatly enhances resistance to surface initiated fatigue cracking in peened materials.

The key parameters in the shot peening induced surface toughening are the magnitude of the stress and the depth of the near surface-compressed plastic zone [30,31]. Over the years, exhaustive empirical optimization of peening intensity for surface toughening in a multitude of applications, varying from dental picks to turbine engine components, has been successfully pursued. Although destructive techniques [33,34] for profiling the underlying compressive stress/strain magnitude and penetration depth have been used, direct nondestructive techniques for probing these key parameters on the required small spatial scale have been lacking.

In recent years, high intensity/energy synchrotron radiation has begun to be used for deeply penetrating X-ray diffraction strain profiling [5–11]. Even in these techniques, however, the elongation of the diffraction volume along the beam direction often limited the spatial resolution [5]. In the strain profiling studies discussed here, the incident X-ray beam is carefully aligned, and the diffraction volume is allowed to elongate, parallel to the shot peened surface (see the insets of Figs. 1 and 2). Perpendicular to peened surface, on the other hand, the beam collimation is kept

3
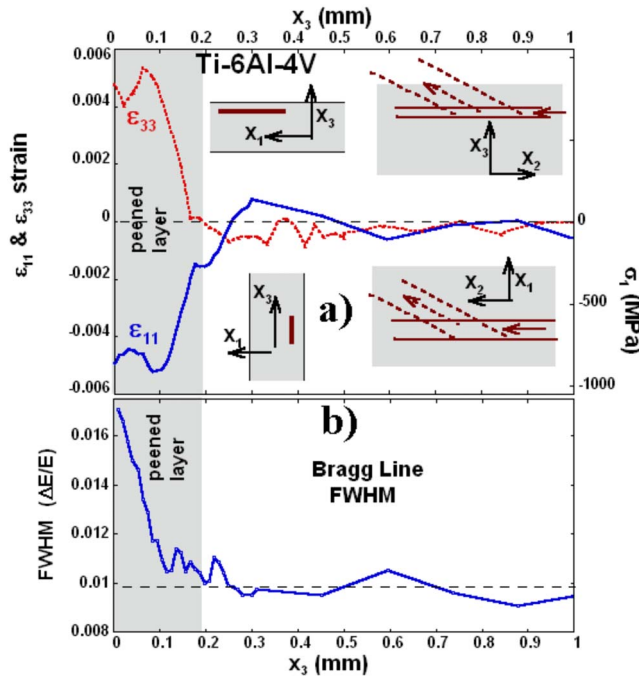
Fig. 2 (*a*) The strain profiles of ε_{33} and ε_{11} in the vicinity of the peened surface layer and the underlying bulk material of the Ti-6Al-4V specimen. The insets illustrate the X-ray scattering geometries for the ε_{33} (top) and ε_{11} (bottom) measurements. Note the stress scale (lower right) uses *E*=118 GPa and ν =0.33 (see text) and σ_1=175×10³ ε_{11} (MPa). (*b*) The Bragg line FWHM profile (for the ε_{11} analysis above) illustrating a strong enhancement in the peening deformed region.

very tight (10–30 μm). With appropriate beam-collimation-slit adjustments, this allows the profiling of both the in-plane and out-of-plane components of the plastic zone strain with extraordinary spatial resolution of 10–30 μm.

Double surface peened Ti-6Al-4V specimen. Ti-6Al-4V is widely used in the internal parts of aerospace gas turbine engines due to its high strength to weight ratio, corrosion resistance, and high temperature property stability [25]. Ordinary fatigue and foreign-object-impact damage induced enhanced fatigue severely limit the lifetime of such no-fail engine components [25]. The introduction of a near surface compressive stress, in many cases by shot peening, is an important and routinely used technique for extending the fatigue lifetimes of crucial and expensive turbine engine components. The processing of the Ti-6Al-4V specimen studied here was similar to that used turbine engine components so that a nondestructive standard characterization of the details of the near surface induced compressive stress region in such materials could be established [25].

In our shot peening studies, the plastic layer is in the x_1-x_2 plane and is perpendicular to x_3 (see the insets of Figs. 1(*a*) and 2(*a*) along with Figs. 6–8). Figure 1 shows the variation of the ε_{33} strain component across the entire depth of an ~5 mm thick Ti-6Al-4V shot peened specimen, along with an inset schematic of the X-ray scattering and sample geometry. Note the symmetric tensile (+) ε_{33} strain on both peened surfaces, along with a balancing compressive (−) strain in the intervening bulk material. It is important to note that the height of the incident X-ray beam (and spatial resolution) in the x_3 direction in these measurements was 20 μm and that a decrease to 10 μm was also achieved with similar (albeit somewhat more scattered) results.

In Fig. 2(*a*), the ε_{33} strain near the peened layer is reproduced, along with the variation of the in-plane ε_{11} strain component. The very different detailed shaping of the diffraction (gauge) volumes

in these two measurements is indicated schematically in the insets of Fig. 2. For the ε_{33} measurement, the incident beam collimation d_i was 20 μm along x_3 (as noted above). In order to increase the diffraction signal, the scattered beam collimation, d_s, was increased to ~200 μm, greatly expanding the gauge volume (GV) along x_2 (parallel to the surface). The collimation width along the x_1 direction, parallel to the peened surface, was ~200 μm. For the ε_{11} measurement, the sample was rotated by 90 deg, the collimation perpendicular to x_3 was 30 μm, and the incident d_i was expanded to ~100 μm (for increased signal), since it was now along the in-plane x_1 direction and d_s was increased to ~300 μm, also to increase the scattered signal.

An experimental point should be noted at this juncture to emphasize the level of detail on which these results should be interpreted. The ε_{33} measurements had a more advantageous geometry allowing a larger GV (expanded in the x_2 direction as noted above) and signal integration over more grains. The stress free d_0 was therefore determined by requiring that the integral of ε_{33} across entire specimen thickness be equal to zero. This same d_0 was then used to determine the ε_{11} values. With this in mind, a modest in-plane ε_{11} compressive strain near the bottom of the plastic zone (i.e., near x_3=0.2 mm) and its contrast with the near zero ε_{33} results at the same depth is a detail worth noting in Fig. 2(*a*). In view of the greater intergranular scatter in the ε_{11} measurements, the authors believe that this detailed observation should not be overinterpreted and, in fact, lies within the interganular scatter. Indeed, we believe that multiple profiling measurements across this interface region in different portions of the specimen would be required to justify this level of interpretation.

With the above caveat noted, the compressive (in-plane) ε_{11} strain and tensile (out-of-plane) ε_{33} strain results in Figs. 1 and 2 are in good accord with the biaxial in-plane stress expected in the plastically deformed shot peened layer [5,29–32]. For biaxial symmetry, ε_{11}=ε_{22} and σ_1=σ_2, where σ_i is the stress in the ith direction. In this case,

$$\sigma_1 = \left[\frac{E}{(1+\nu)(1-2\nu)}\right]\{\varepsilon_{11} + \nu\varepsilon_{33}\} \qquad (1a)$$

and

$$\sigma_3 = \left[\frac{E2\nu}{(1+\nu)(1-2\nu)}\right]\varepsilon_{33}\left\{\frac{(1-\nu)}{2\nu} + \frac{\varepsilon_{11}}{\varepsilon_{33}}\right\} \qquad (1b)$$

where ν is Poisson's ratio and E is Young's modulus. For Ti-6Al-4V, ν=0.33 and one obtains

$$\sigma_3 = \left[\frac{3E}{2}\right]\varepsilon_{33}\left\{1 + \frac{\varepsilon_{11}}{\varepsilon_{33}}\right\} \qquad (2)$$

Since the experimental results in Fig. 2 indicate that, to a very good approximation, $\varepsilon_{11} \sim -\varepsilon_{33}$, one has $\sigma_3 \sim 0$. This is not at all unexpected in view of the free surface in the x_3 direction. Indeed, in general, σ_3=0 leads to

$$\frac{\varepsilon_{11}}{\varepsilon_{33}} = -\frac{1-\nu}{2\nu} \qquad (3a)$$

and

$$\sigma_1 = \varepsilon_{11}\left[\frac{E}{(1-\nu)}\right] \qquad (3b)$$

the former of which reduces to the observed $\varepsilon_{11} \sim -\varepsilon_{33}$ for ν =0.33. Further, using E=118 GPa for Ti-6Al-4V, one obtains the in-plane stress scale σ_1=175×10³ ε_{11} (MPa), which is shown in the right hand scale of Fig. 2(*a*). It is important to reiterate here that this stress calculation is an approximation, as noted earlier, since it ignores the differences between the crystallographic-direction dependent elastic constants and bulk elastic properties [27].

As noted above, the depth of the compressive stress region is

4
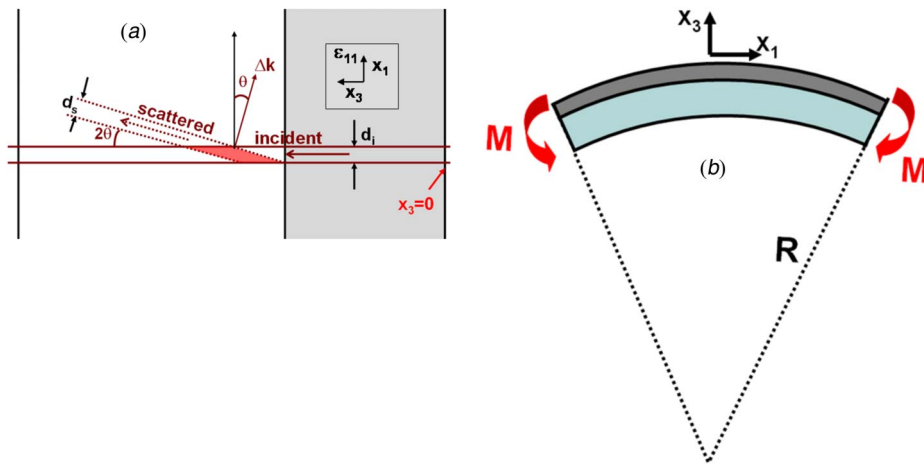
Fig. 3 (*a*) Schematic of placket bending with convex peened surface up. (*b*) Scattering geometries for the ε_{11} measurement case $2\theta=12$ deg and $d_i=d_s=40$ μm. For the ε_{33} case, 2θ $=6$ deg and $d_i=30$ μm and $d_s=200$ μm.

important in determining the near surface toughening resulting from the shot peening treatment. For this Ti-6Al-4V specimen, the depth of this compressional region, as measured by our X-ray diffraction technique, is ~180 μm. Referring to the surface profiling measurements shown in Fig. 8, we note that the plastic lip at the edge of the specimen is also ~180 μm. This correlation suggests the possibility that optical profiling measurements of such lips might provide a useful factory floor measurement of the important depth parameter of the compressional plastic zone. Here, a calibration standard of the same material with a well-defined edge would be peened simultaneously with a structural component part. In the steel, the specimen discussed below a similar correlation will be noted. More work on this augmentation of the traditional Almen strip curvature calibration of peening intensity (noted below) would appear justified [29].

In Fig. 2(*b*), a plot of the fitted hcp 110-line FWHM for the ε_{11} measurements versus the position inside the Ti-6Al-4V is shown on the same x scale as Fig. 2(*a*). The systematic line broadening in the peened plastic zone is dramatic compared to the linewidth in the specimen interior (i.e., for $x_3 > 0.3$ mm). Material contributions to an increase in the Bragg linewidth come from intragrain microstrains and from decrease in the coherent scattering domain size (which is less than the grain size) [24–26]. In EDXRD, the largest linewidth contribution comes from electronic broadening of the detector [26], the nominal value of which can be seen by the FWHM in the specimen interior ($x_3 > 0.3$ mm in Fig. 2(*a*)). In principle, the Bragg line broadening in the plastic zone can involve both a decrease in the grain (and coherent X-ray domain) size and microstrain effects and a more detailed analysis of these two contributions will be discussed elsewhere. In practice, recent work [35–37] has demonstrated dramatic grain size diminution, down to a nanolevel, upon approaching a shot peened surface. This process can also be viewed as the peening impacts creating a steep dislocation gradient [38] in which dislocation coalescence increasingly breaks down the grain size as a surface is approached. At present, therefore, we interpret the dramatic rise in the Bragg line FWHM, approaching the peened surface (see Fig. 2(*b*)), as evidenced of such a dislocation gradient and the grain size refinement as the plastic zone is entered and the surface approached. It is worth noting again that the point-to-point intergranular scatter in the FWHM data is larger in the interior of the specimen due to a larger contribution from intragrain strains in the larger grain size interior region. Our group has observed similar intergranular scatter disparities between the plastic zone near fatigue crack tips and unstrained, larger grain regions in ongoing studies of aluminum-alloy specimens [39].

Single Surface Peened 1070 Spring Steel Specimen With Bending Curvature. We will now consider a second shot peening application of this X-ray strain profiling technique with differing boundary conditions. In this case, intense shot peening was applied to just one surface of a 1070 spring steel specimen of ~4 mm thickness. It should be noted that the ~6 mm diameter of the peening shot (see Appendix) is much larger than used for typical industrial applications. However, since the depth of the plastic zone scales with the shot diameter, the large diameter shot does allow the study of a plastic-compressed zone with a much larger spatial scale. Here, as in the case of a bimetallic strip when heated, the stress differential between the two layers (the peened and bulk) introduces a bending moment M and a curvature of the sample (see Fig. 3(*a*) for an exaggerated schematic of this curvature). Indeed, the degree of such curvature in standard stress-relieved 1070 steel, "Almen strips" are routinely used as an empirical measure to determine the peening intensity in industrial applications [29]. The choice of a 1070-steel specimen for the present study was motivated by its status as a standard calibration material in the shot peening field.

ε_{11} strain measurements on this sample were performed by our group [5], in the geometry illustrated in Fig. 3(*b*), and the results are shown in Fig. 4(*a*). The compressive ε_{11} strain in the plastically deformed peened layer and the linear spatial variation in the elastic strain response in the underlying material [5] are strikingly apparent in Fig. 4(*a*). The thickness of the peened layer in this specimen was thick enough that the orientation of the diffraction volume, with its elongated direction along x_3, resulted in only modest rounding of the peened-layer/substrate interface.

Also shown in Fig. 4(*a*) is a recent measurement of the ε_{33} strain collected in the geometry shown in the inset of Fig. 2(*a*). The analogous behavior, but opposite signs, of the ε_{33} strain (relative to the ε_{11} strain) is clear upon comparing the two strain component curves in Fig. 4(*a*). Indeed, the linear spatial variation in the bending-moment-elastic-response portions of the ε_{33} and ε_{11} curves indicates a specimen curvature radii in the 1700–1800 mm range, consistent (with experimental uncertainties) with the three-point macroscopic curvature measurement of 1650 mm. It should be noted that the spatial resolution of the ε_{33} strain measurement (along the x_3 direction) is 30 μm, so that essentially no finite-gauge-volume rounding is present in these data.

As in the Ti6Al-4V specimen discussed above, theoretical expectations, and the qualitative mirror-image-type relationship between the ε_{11} and ε_{33} strain behaviors for this 1070-steel specimen, support the expectation of biaxial stress. Accordingly, using

5
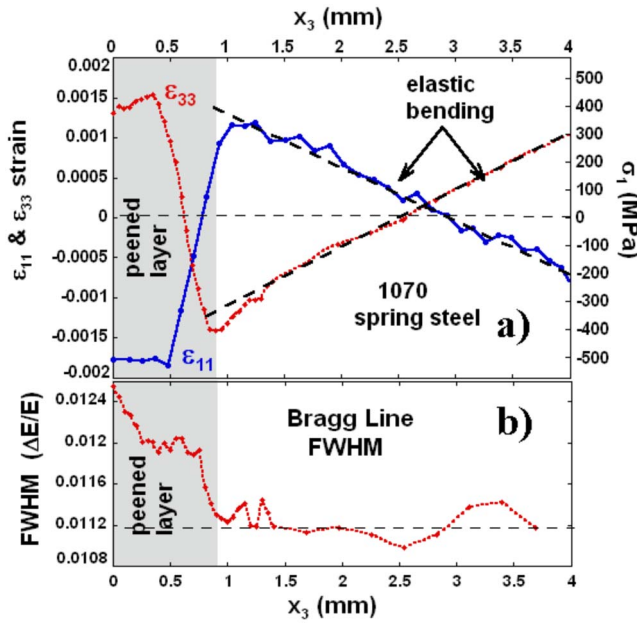
Fig. 4 (*a*) The strain profiles of ε_{33} and ε_{11} across the entire thickness of a heavily peened 1070 spring steel specimen. Note the stress variation on the right and scale corresponds to the ε_{11} (blue) curve with and $\sigma_1 = 286 \times 10^3 \ \varepsilon_{11}$ (MPa). (*b*) The Bragg line FWHM profile (for the ε_{11} analysis above) across the heavily peened 1070 spring steel specimen.

Eq. (3*b*), with Poisson's ratio of $\nu = 0.3$ and $E = 200$ GPa, the approximate equivalent in-plane $\sigma_1 = 286 \times 10^3 \ \varepsilon_{11}$ (MPa) stress scale has been included on the right in Fig. 4(*a*). The maximum near surface compression is $\sigma_1(\max) \sim 530$ MPa and the formal depth of the compressive ($-$) stress region is $\sim 0.6–0.7$ mm. The onset of the deviation from the linear elastic bending behavior clearly indicates that the peening influence extends to a greater depth of ~ 0.9 mm. The results on this peened steel specimen emphasize that both the compressive strain in the localized plastic surface region and the complex long-range elastic response of the underlying bulk material can be characterized in great detail with the nondestructive synchrotron X-ray technique used here.

In Fig. 4(*b*), a plot of the fitted fcc-Fe 321-line FWHM for the ε_{33} measurements versus the position inside this 1070 peened specimen is shown on the same *x* scale as Fig. 4(*a*). Again a systematic line broadening in the peened plastic zone is observed relative to the underlying elastically strained region. Although clearly defined, the FWHM plastic zone broadening effect in this 1070-steel specimen appears to be less dramatic than in the Ti-6Al-4V specimen discussed above. Modeling of the dislocation density gradient produced in shot peening has been characterized by the ratio v/r, where v and r are the shot velocity and radius, respectively [38]. In view of the large shot diameter used for this 1070-steel specimen, one might expect smaller dislocation density and strain rate plasticity effects. A systematic study is clearly required before any real conclusions on such issues can be made.

3.2 Tensile Stress Material Breakdown: Fatigue Crack Wake Effect. In contrast to the compression effect in the shot peening examples above, fatigue crack growth occurs as the result of localized tensile (positive) stresses, concentrated at the crack tip [40]. The formal singular elastic enhancement in the local tensile stress, which occurs near a fatigue crack tip, naturally leads to strain localization, strong plastic deformation, and localized fracture in a region around the tip [40]. The propagation of the crack tip then leaves behind it a deformed plastic wake at the crack face, created by tensile fracture. The large tensile stress (along the *y*

direction, with the crack propagation in the *x* direction) induces a local *y* elongation and a transverse *x-z* contraction of the material. These interior strains are accompanied by a surface "necking" deformation as seen in the surface profile in the Fig. 9 for a fatigue crack in 4140-steel specimen. The plasticity-induced necking upon approaching the crack face is clear from this nonlinear surface dimpling (Fig. 9). Indeed, varying the loading will leave varying spatial extents of the concave surface dimple along the crack [6,7]. It should be noted that the choice of 4140 steel for these studies was made due to its utility in naval applications, and its small grain size, which enables small GV studies of the fatigue crack strain fields [6,7].

In our synchrotron-based fatigue crack strain profiling, the GV was tailored to the sample geometry, in which the crack was aligned closely parallel to the *x* direction. The ε_{yy} measurements had a rectangular *x-y* cross section of $200 \times 60 \ \mu\text{m}^2$. The ε_{xx} measurements had an *x-y* cross section of $\sim 100 \times 60 \ \mu\text{m}^2$. The *z-y* gauge volume cross section was an elongated regular parallelogram, the maximal *z* extent being $\sim 300 \ \mu\text{m}$ [5–7]. It is worth noting that Ref. [7] utilizes a smaller $50 \times 50 \ \mu\text{m}^2$ *x-y* GV to profile the crack tip strain fields in similar specimens.

The schematic inset in Fig. 5(*a*) illustrates the fatigue crack with the conventional choices of *x* axis parallel to the crack, *y* axis perpendicular to the crack, and the coordinate origin at the crack tip. The variation of ε_{yy} (ε_{xx}) crossing the crack perpendicularly along the *y* direction (at $x = -2$ mm behind the tip) for a fatigue cracked 4140-steel specimen is shown in Fig. 5(*a*). We wish to draw attention to the region of strongly nonlinear plastic flow in the strain results. Specifically, the sharp negative (positive) peak in ε_{yy} (ε_{xx}), labeled 1 (and shaded) in Fig. 5(*a*), occurring within a region of ± 0.15 mm of the center of the crack ($y = 0$) should be noted. The results in Fig. 5(*a*) clearly show that in this near-crack plastic wake region, the strain anomaly is highly anisotropic, with $\varepsilon_{yy}/\varepsilon_{xx} \sim -0.7$. It should be noted that this phenomenon is morphologically typical of the near-crack behavior for all of the fatigued specimens studied by our group [6,7].

Assuming in this case that $\sigma_y = 0$ in the proximity of the crack surface (at $y = 0$), one finds

$$\varepsilon_{zz} = -\varepsilon_{xx} - \left(\frac{1}{\nu} - 1\right)\varepsilon_{yy} \qquad (4)$$

Using the experimental observation $\varepsilon_{yy}/\varepsilon_{xx} \sim -0.7$ and $\nu = 0.3$, one finds $\varepsilon_{zz}/\varepsilon_{xx} \sim -0.63$, which is close to (but depressed from) $\varepsilon_{xx}/\varepsilon_{zz}$ biaxiality. Such a depression is not unexpected in view of the proximity of free surfaces at $z = \pm 2$ mm from this center-specimen measurement. Moreover, at the crack tip, where this wake zone was created, there is a real physical difference between the strain parallel (ε_{xx}) and transverse (ε_{zz}) to the crack propagation direction. The stresses, within the $\sigma_y = 0$ assumption, are

$$\sigma_x = \left[\frac{E}{(1+\nu)}\right]\{\varepsilon_{xx} - \varepsilon_{yy}\} \qquad (5a)$$

and

$$\sigma_z = \left[\frac{-E}{(1+\nu)\nu}\right]\{\varepsilon_{yy} + \nu\varepsilon_{xx}\} \qquad (5b)$$

Again, inserting $\varepsilon_{yy}/\varepsilon_{xx} \sim -0.7$ with $\nu = 0.3$ in these expressions, one obtains $\sigma_x = 1.31E \ \varepsilon_{xx}$ and $\sigma_z = 1.03E \ \varepsilon_{xx}$. Using $E = 200$ GPa, the maximal stresses in the wake zone are $\sigma_x = 287$ MPa and $\sigma_z = 225$ MPa. Here, it should be reiterated that these stress estimates are nominal since the triaxial stress state in the wake region is, as argued above, almost certainly more complicated than biaxial. Accordingly, a stress scale has been explicitly omitted from Fig. 5(*a*) to emphasize that while our results do demonstrate a dramatic wake effect they are limited to two strain components. In this case, the present EDXRD results motivate a precise spatial and physical-effect focus for the more powerful, but more difficult, constant wavelength type studies where the true triaxial stress
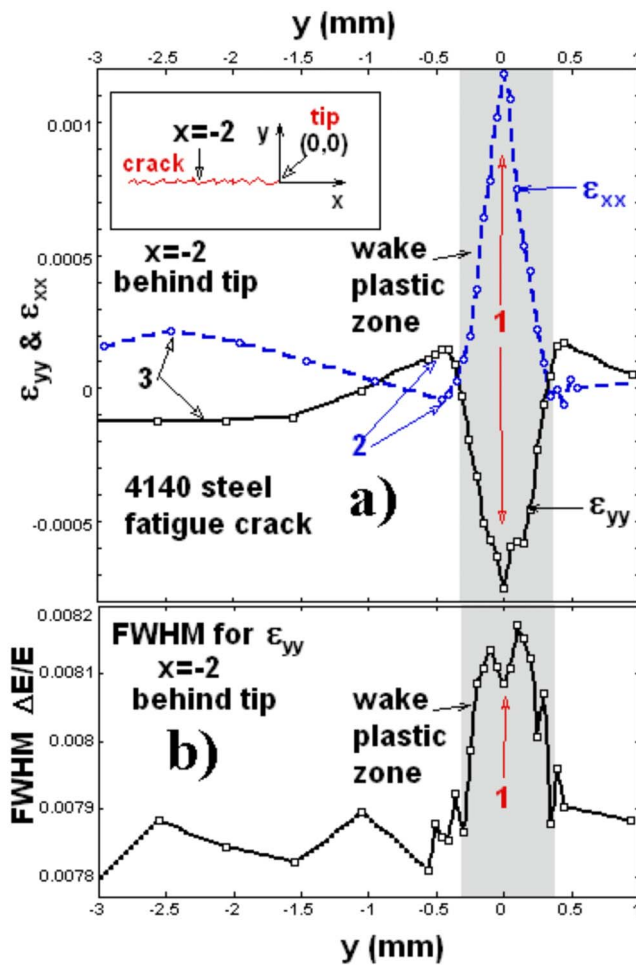
Fig. 5 (*a*) Strain profiles along the *y* direction (crossing the crack perpendicularly) at a coordinate *x*=−2 mm (i.e., 2 mm behind the tip) for a fatigued 4140 specimen. The residual ε_{yy} (solid black line) and ε_{xx} (dashed blue line) strain components are shown. Note the sharp anomalies (see Label 1 in figure) located at the crack, and the plastic wake zone shaded. The broader background variation (see Labels 2 and 3 in figure) farther from the crack. (*b*) The Bragg line FWHM profile (for the ε_{yy} analysis above) across the wake region of the fatigue crack.

tensor can be determined [14–22].

Thus, these results show strain localization, resulting from tensile failure, in a narrow plastic zone immediately on both sides of a fatigue crack. In this plastic wake region, the anisotropic large ε_{xx} contraction and smaller ε_{yy} expansion indicate the anisotropic residual stress after tensile fracture. The longer range strain oscillations (labeled 2 and 3 in Fig. 5(*a*)) appearing to be elastic strain responses bordering the crack wake are not directly relevant to the central focus of this paper and will be discussed at length elsewhere.

Recall that the plastic deformations, in the previous section's shot peening examples, were accompanied by Bragg line broadening. Accordingly, a plot of the FWHM of the 321-Bragg line, perpendicularly crossing the fatigue crack plastic wake zone for this 1040 steel specimen, is shown in Figure 5(*b*). The Bragg line broadening, evidenced by the increase in the FWHM, in the plastic wake zone is again abundantly clear. The importance of the dislocation density in defining the plastic zone near a fatigue crack tip has been discussed at length in the literature [40,41]. Thus, in this tensile example, a combination of intragrain dislocation-

induced strains and coalesced dislocations reducing the effective grain size is presumably responsible for the Bragg line broadening in the wake plastic zone.

4 Conclusion

Detailed experimental examples of strain localization phenomena, which accompany strong gradients in compression and tension loading of metals, have been presented here. This work, along with other work [5–22], demonstrates the power the expanding group of high-energy synchrotron X-ray diffraction techniques for nondestructive, fine mesh sectioning of the nonlinear strain gradients in applied material systems. In particular, the detailed variation in magnitude and anisotropy of the strain can be mapped both in small-scale plasticity regions and deep in the bulk of test specimens. Interestingly, the strain anisotropy's near the shot peened and fatigue crack-face near surfaces are mirror images of each other (i.e., have opposite strain signs). This is consistent with the fact that they were produced by stress gradients of opposite (compressive and tensile) signs. Interestingly, also the small spatial scale cross sectioning of the Bragg line broadening effects in both the compression and tension induced plastic zones provides another method of mapping plastic deformation zones in materials besides the strain gradient variation. Such exhaustive nondestructive strain profiling results can play a crucial role in advancing the state of engineering design and realistic model construction/validation.

On an applied note, we have observed a good correlation between the width of plastically deformed lip protruding at the edge of a shot peened test specimen (see Appendix), and the depth of the peening induced compressive plastics zone as measured by X-ray diffraction. This correlation suggests that optical profiling measurements on the edges of test specimens could provide peening shop-floor estimates of the compressive zone depth. Indeed, the same optical profiling instrumentation could be used to provide a measure of the Almen strip curvature, which is much more revealing than the conventional three-point curvature measurement.

Acknowledgment

Appendix: Surface Structures Accompanying Plastic Deformations

1 Surface Measurements on Shot Peened Materials

If for no other reason than that surface measurements are much more accessible, it is useful to correlate surface manifestations of plastic deformations with the interior X-ray strain field profiling discussed in this paper. In Fig. 6, we show micrographs qualitatively illustrating the surface deformations induced by shot peening. In Fig. 6(*a*), and micrograph of the shot peened surface (x_1-x_2
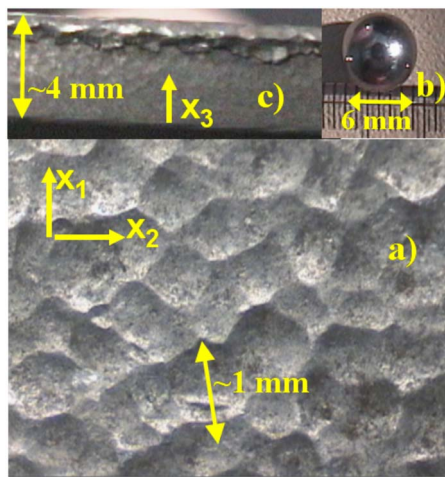
Fig. 6 Micrographs related to 1070-steel shot peened specimen illustrating the qualitative peening induced surface deformations. (*a*) **The shot peened surface** (x_1-x_2) **surface showing the** x_1-x_2 **surface craters caused by the ballistic impacts of shot incident from the** x_3 **direction.** (*b*) **The** $r = 3$ **mm radius shot used in the peening process with a millimeter scale included for reference.** (*c*) **An edge view of the 1070-steel peened specimen showing the bulging of the peened layer forming a protruding lip** (**at top of figure**) **at the edge.**

plane) of a 1070-steel specimen clearly shows the dense impact cratering typical for shot impingent along the x_3 direction. Figure 6(*b*) shows a picture of the large radius, $r = 3$ mm, shot used to peen the specimen. Although such large shot is atypical for most shot peening applications, it provides a useful illustration of the

processes and structures involved. In Fig. 6(*c*) the lateral plastic flow for this specimen can be seen from the plasticity induced material bulging at the edges of the x_1-x_2 surface [30]. Here, the ~ 4 mm specimen thickness along the x_3 direction can also be seen.

In order to provide quantitative results for the peening induced surface deformations, we have utilized a Zygo New View 5200 optical profiler to perform white light microscopy surface height maps [28]. The surface height mapping results in Fig. 7(*a*), for the x_1-x_2 surface of the 1070-steel specimen, quantitatively demonstrate the impact cratering topography. The line profile (extracted from a cross section of the surface map in Fig. 7(*a*)) shown in Fig. 7(*b*) shows a crater distribution with depths of ~ 30 μm and widths of $\sim 0.3-1.0$ mm. The dotted line in Fig. 7(*b*) is a plot (in the scale of the profile data) of the locus of a circle with a radius equal to that of the peening shot $r = 3$ mm. Interestingly, the detailed curvature of the bottom portions of the craters appears to be quite close to that of the peening shot.

Figure 7(*c*) provides a quantitative mapping of the edge bulging (see Fig. 6(*c*)) of the lateral plastic flow for the 1070-steel peened specimen. The plastic bulge is seen to protrude ~ 120 μm beyond the edge and to have a thickness of ~ 0.7 mm. This thickness correlates well with the compressive strain region, as measured by X-ray diffraction, in the interior of the 1070-steel peened specimen discussed in the text.

In Fig. 8, a similar edge-on surface height map for the aerospace alloy, Ti-6Al-4V, peened specimen is shown. The bulging morphology is the same as in the steel specimen, but with much smaller spatial scale (height ~ 55 μm, and thickness ~ 180 μm) due to the much smaller peening shot and intensity (relative to the 1070-steel specimen). Here, again the thickness of the edge bulge correlates well with the near surface region of compression determined from the X-ray depth profiling strain measurements discussed in the main text.
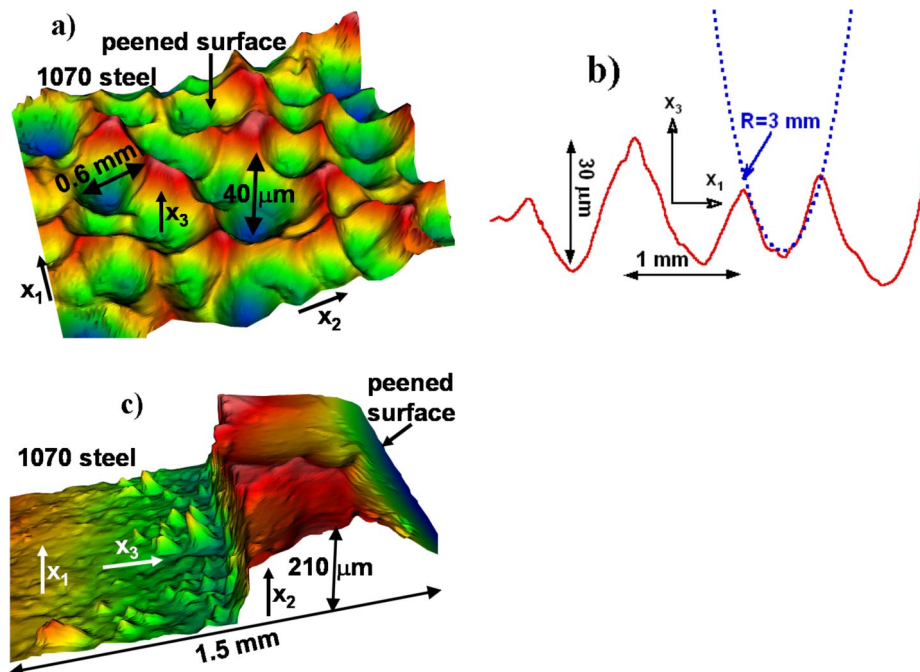
Fig. 7 Surface height mapping results providing quantitative surface deformation results for the shot peened 1070-steel specimen. (*a*) **3D surface height topographic map (tilted for perspective) of the peened** x_1-x_2 **surface (see also Fig. 6(*a*)).** (*b*) **A selected line profile from the data set from the previous figure with the appropriate vertical and horizontal length scales provided. A plot (dotted line) of a circle of radius** $r = 3$ **mm equal to that of the peening shot is shown (see also Fig. 6(*b*)).** (*c*) **A surface map of the edge specimen illustrating the bulging of the peened layer to form a lip (see also Fig. 6(*c*)) at the edge.**

8
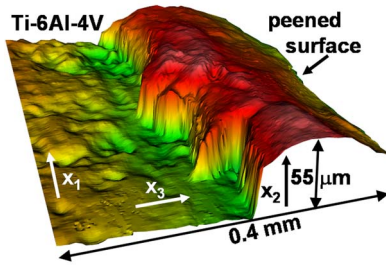
Fig. 8 Surface map of the edge of the Ti-6Al-4V peened specimen showing the bulging of the plastic peened layer at the edge. Note that the spatial scale of the peening effect is dramatically smaller than that illustrated in the previous figure.
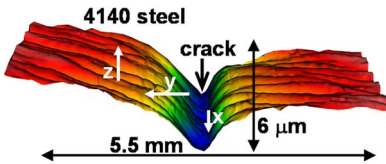
Fig. 9 3D perspective surface topographic map of the surface height in the vicinity of a fatigue crack in a 4140-steel specimen. Note the transverse "necking," inward plastic flow, on the flanks of the crack due to the localized material yielding in tension.

2 Surface Measurements on a Fatigue Crack Plastic Wake Region

In the shot peening examples above compression induced failure caused a bulging at the materials edge. Failure in tension on the other hand should induce an inward plastic flow or a necking in the localized region of tensile failure. For a propagating fatigue crack, a tensile failure occurs at the crack tip leaving behind a wake of plastically deformed material at the crack faces [41]. The surface height profile in Fig. 9 shows the "necking" or surface dimpling effect in the vicinity of a fatigue crack. The plasticity-induced necking upon approaching the crack face is clear from this nonlinear surface dimpling. Indeed, varying load levels have been shown to produce varying spatial extents of the concave surface dimple along the crack [6,7].

References

[1] Sharon, E., Marder, M., and Swinney, H., 2004, "Geometry and Elasticity of Strips and Flowers," Am. Sci., **92**, pp. 254–261.

[2] Audoly, B., and Boudaoud, A., 2003, "Self-Similar Structures Near Boundaries in Strained Systems," Phys. Rev. Lett., **91**, p. 086105.

[3] England, P., and Molnar, P., 1997, "Active Deformation of Asia: From Kinematics to Dynamics," Science, **278**, pp. 647–650.

[4] Qin, R., and Buck, W., 2005, "Effect of Lithospheric Geometry on Rift Valley Relief," J. Geophys. Res., **110**, p. B03404.

[5] Croft, M., Zakharchenko, I., Zhong, Z., Gulak, Y., Hastings, J., Hu, J., Holtz, R., DaSilva, M., and Tsakalakos, T., 2002, "Strain Field and Scattered Intensity Profiling With Energy Dispersive X-Ray Scattering," J. Appl. Phys., **92**, pp. 578–586, and references therein.

[6] Croft, M., Zhong, Z., Jisrawi, N., Zakharchenko, I., Holtz, R., Gulak, Y., Skaritka, J., Fast, T., Sadananda, K., Lakshmipathy, M., and Tsakalakos, T., 2005, "Strain Profiling of Fatigue Crack Overload Effects Using Energy Dispersive X-Ray Diffraction," Int. J. Fatigue, **27**, pp. 1408–1419, and references therein.

[7] Croft, M., Jisrawi, N., Zhong, Z., Holtz, R., Sadananda, K., Skaritka, J., and Tsakalakos, T., 2007, "Fatigue History and In-Situ Loading Studies of the Overload Effect Using High Resolution X-Ray Strain Profiling," Int. J. Fatigue, **29**(9–11), pp. 1726–1736.

[8] Steuwer, A., Santistebban, J., Turski, M., Withers, P., and Buslap, T., 2004, "High-Resolution Strain Mapping in Bulk Samples Using Full-Profile Analysis of Energy-Dispersive Synchrotron X-Ray Diffraction Data," J. Appl. Crystallogr., **37**, pp. 883–889.

[9] Steuwer, A., Santisteban, J., Turski, M., Withers, P., and Buslaps, T., 2005, "High-Resolution Strain Mapping in Bulk Samples Using Full-Profile Analysis of Energy Dispersive Synchrotron X-Ray Diffraction Data," Nucl. Instrum. Methods Phys. Res. B, **238**(1–4), pp. 200–204.

[10] Korsunsky, A., Collins, S., Owen, R., Daymond, M., Achtioui, S., and James, K., 2002, "Fast Residual Stress Mapping Using Energy-Dispersive Synchrotron X-Ray Diffraction on Station 16.3 at the SRS," J. Synchrotron Radiat., **9**, pp. 77–81.

[11] James, M., Hattingh, D., Hughes, D., Wei, L.-W., Patterson, E., Quinta Da Fonseca, J., 2004, "Synchrotron Diffraction Investigation of the Distribution and Influence of Residual Stresses in Fatigue," Fatigue Fract. Eng. Mater. Struct., **27**, pp. 609–622.

[12] Jones, J., Motahari, S., Varlioglu, M., Lienert, U., Bernier, J., Hoffman, M., and Ustundag, E., 2007, "Crack Tip Process Zone Domain Switching in a Soft Lead Zirconate Titanate Ceramic," Acta Mater., **55**, pp. 5538–5548.

[13] Martins, R., Lienert, U., Margulies, L., and Pyzalla, A., 2005, "Determination of the Radial Crystallite Microstrain Distribution Within an AlMg3 Torsion Sample Using Monochromatic Synchrotron Radiation," Mater. Sci. Eng., A, **402**, pp. 278–287.

[14] Haeffner, D., Almer, J., and Lienert, U., 2005, "The Use of High Energy X-Rays From the Advanced Photon Source to Study Stresses in Materials," Mater. Sci. Eng., A, **399**, pp. 120–127.

[15] Margulies, L., Lorentzen, T., Poulsen, H., and Leffers, T., 2002, "Strain Tensor Development in a single grain in the bulk of a Polycrystal Under Loading," Acta Mater., **50**, pp. 1771–1779.

[16] Martins, R., Margulies, L., Schmidt, S., Poulsen, H., and Leffers, T., 2004, "Simultaneous Measurement of the Strain Tensor of 10 Individual Grains Embedded in an Al Tensile Sample," Mater. Sci. Eng., A **387–389**, pp. 84–88.

[17] Behnken, H., 2000, "Strain-Function Method for the Direct Evaluation of Intergranular Strains and Stresses," Phys. Status Solidi A **177**, pp. 401–418.

[18] Wang, Y., Lin-Peng, R., and McGreevy, R., 2001, "A Novel Method for Constructing the Mean Field of Grain-Orientation-Dependent Residual Stress," Philos. Mag. Lett., **81**(3), pp. 153–163.

[19] Bernier, J., and Miller, M., 2006, "A Direct Method for the Determination of the Mean Orientation-Dependent Elastic Strains and Stresses in Polycrystalline Materials From Strain Pole Figures," J. Appl. Crystallogr., **39**(3), pp. 358–368.

[20] Miller, M., Bernier, J., Park, J., and Kazimirov, A., 2005, "Experimental Measurement of Lattice Strain Pole Figures Using Synchrotron X-rays," Rev. Sci. Instrum., **76**, p. 113903.

[21] Han, T., and Dawson, P., 2005, "Lattice Strain Partitioning in a Two-Phase Alloy and Its Redistribution Upon Yielding," Mater. Sci. Eng., A, **405**, pp. 18–33.

[22] Barton, N., and Dawson, P., 2001, "On the Spatial Arrangement of Lattice Orientations in Hot-Rolled Multiphase Titanium," Modell. Simul. Mater. Sci. Eng., **9**, pp. 433–463.

[23] see, Hertzberg, R., 1983, *Deformation and Fracture Mechanics of Engineering Materials*, Wiley, New York, Chap. 1.

[24] Gerward, L., Morup, S., and Topsoe, H., 1976, "Particle Size and Strain Broadening in Energy-Dispersive X-Ray Powder Patterns," J. Appl. Phys., **47**, pp. 822–825.

[25] Otto, J. W., 1997, "On the Peak Profiles in Energy-Dispersive Powder X-ray Diffraction with Synchrotron Radiation," J. Appl. Crystallogr., **30**, pp. 1008–1015.

[26] Ellmer, K., Mientus, R., Weiss, V., and Rossner, H., 2003, "In Situ Energy-Dispersive X-Ray Diffraction System for Time-Resolved Thin-Film Growth Studies," Meas. Sci. Technol., **14**, pp. 336–345.

[27] Brunoy, G., and Dunnz, B., 1997, "The Precise Measurement of Ti6A14V Microscopic Elastic Constants by Means of Neutron Diffraction," Meas. Sci. Technol., **8**, pp. 1244–1249.

[28] Deck, L., and de Groot, P., 1994, "High-Speed Noncontact Profiler Based on Scanning White-Light Interferometry," Appl. Opt., **33**, pp. 7334–7338.

[29] Leghorn, G., 1957, "The Story Of Shot Peening," J. Am. Soc. Nav. Eng., p. 654.

[30] Wohlfahrt, H., 1984, "The Influence of Peening Conditions on the Resulting Distribution of the Residual Stress," *Proceedings of the Second International Conference on Shot Peening* Chicago, Paper No. 511984, pp. 316–331.

[31] Al-Hassani, S., 1981, "Mechanical Aspects of Residual Stress Development in Shot Peening," First International Conference on Shot Peening-1, Paris, pp. 593.

[32] Evans, R., 2002, "Shot Peening Process: Modelling, Verification, and Optimisation," Mater. Sci. Technol. **18**, pp. 831–839.

[33] See the review by Prime, M., 1999, "Residual Stress Measurement by Successive Extension of a Slot: The Crack Compliance Method," Appl. Mech. Rev., **52**, pp. 75–96.

[34] See the review by Withers, P., and Bhadeshia, H., 2001, "Residual Stress. I-Measurement Techniques," Mater. Sci. Technol. **17** pp. 355–365 and references therein.

[35] see Zhuang, W. and Wicks, B., 2003, "Mechanical Surface Treatment Technologies for Gas Turbine Engine Components," ASME J. Eng. Gas Turbines Power, **125**, pp. 1021–1025, and references therein.

[36] Wang, Y. M., Wang, K., Pan, D., Lu, K., Hemker, K., and Ma, E., 2003, "Microsample Tensile Testing of Nanocrystalline Copper," Scr. Mater., **48**, pp. 1581–1586.

[37] Zhang, X. N., Zhang, B. H., Zhao, C. L., Tao, N. R., and Wang, Y. M., 2007, unpublished.

[38] Xinling, M., Wei, W., and Wei, Y., 2003, "Simulation for Surface Self-Nanocrystallization Under Shot Peening," Acta Mech. Sin., **19**, pp. 1614–3116.

[39] unpublished.

[40] Suresh, S., 1991, *Fatigue of Materials*, Cambridge University Press, Cambridge, Chap. 5 and references therein.

[41] see Sadananda, K., Vasudevan, A. K., Holtz, R. L., and Lee, E. U., 1999, "Analysis of Overload Effects and Related Phenomena," Int. J. Fatigue, **21**, pp. S233–S246, and references therein.